Hot Paper

Multifunctional Photoelectroactive Materials for Optoelectronic Applications Based on Thieno[3,4-b]pyrazines and Thieno[1,2,5]thiadiazoles

Mattia Zangoli,[a, b] Filippo Monti,*[a] Alberto Zanelli,[a] Martina Marinelli,[c] Soraia Flammini,[a, d] Nicol Spallacci,[a] Anna Zakrzewska,[e] Massimiliano Lanzi,[c] Elisabetta Salatelli,[c] Filippo Pierini,[e] and Francesca Di Maria*[a, b]

In this study, we introduce a novel family of symmetrical thiophene-based small molecules with a Donor-Acceptor-Donor structure. These compounds feature three different acceptor units: benzo[c][1,2,5]thiadiazole (Bz), thieno[3,4-b]pyrazine (Pz), and thieno[1,2,5]thiadiazole (Tz), coupled with electron donor units based on a carbazole-thiophene derivative. Using Density Functional Theory (DFT), we investigate how the molecular geometry and strength of the central acceptor unit impact the redox and spectroscopic properties. Notably, the incorporation of Pz and Tz moieties induces a significant redshift in the absorption and emission spectra, which extend into the near-infrared (NIR) region, simultaneously reducing their energy gaps ($\sim$1.4–1.6 eV). This shift is attributed to the increased coplanarity of the oligomeric inner core, both in the ground (S_0) and excited (S_1) states, due to the enhanced quinoidal character as supported by bond-length alternation (BLA) analysis. These structural changes promote better π-electron delocalization and facilitate photoinduced charge transfer processes in optoelectronic devices. Notably, we show that Pz- and Tz-containing molecules exhibit NIR electrochromic behavior and present ambivalent character in bulk heterojunction (BHJ) solar cells. Finally, theoretical calculations suggest that these molecules could serve as effective two-photon absorption (2PA) probes, further expanding their potential in optoelectronic applications.

[a] Dr. M. Zangoli, Dr. F. Monti, Dr. A. Zanelli, S. Flammini, N. Spallacci, Dr. F. Di Maria
Consiglio Nazionale delle Ricerche (CNR)
Istituto per la Sintesi Organica e la Fotoreattività (ISOF)
via Piero Gobetti 101, 40129 Bologna (Italy)
E-mail: filippo.monti@isof.cnr.it
       francesca.dimaria@isof.cnr.it

[b] Dr. M. Zangoli, Dr. F. Di Maria
CLAN-Center for Light Activated Nanostructures
Istituto ISOF-CNR
40129 Bologna (Italy)

[c] Dr. M. Marinelli, Prof. M. Lanzi, Prof. E. Salatelli
Department of Industrial Chemistry "Toso Montanari"
University of Bologna
Viale Risorgimento 4, 40136 Bologna (Italy)

[d] S. Flammini
RCCS Ospedale Policlinico San Martino
16132 Genova (Italy)

[e] A. Zakrzewska, Prof. F. Pierini
Department of Biosystems and Soft Matter, Institute of Fundamental Technological Research
Polish Academy of Sciences
ul. Pawinskiego 5B, 02-106 Warsaw (Poland)

Supporting information for this article is available on the WWW under https://doi.org/10.1002/chem.202303590

Introduction

Conjugated small molecules have become crucial components in a diverse array of optoelectronic devices, such as organic solar cells, light-emitting diodes, electrochromic devices, and field-effect transistors.[1] The appeal of small molecules stems from their precise structure, offering exceptional control for fine-tuning optical, redox, and electronic properties.[2] Within the realm of conjugated small molecules, thiophene-based oligomers have a prominent role.[3] These materials have been shown to excel in multiple aspects crucial for optoelectronic devices, including their conjugation, tunable electro-optical properties, processability, stability, and versatility in donor-acceptor roles.[4] Importantly, the electro-optical properties of thiophene-based materials can be significantly influenced by the modification of their chemical structure. This includes varying the length and branching of alkyl side chains, changing the nature and position of substituents on the thiophene rings, introducing different heteroatoms (*e.g.*, nitrogen, sulfur) into the molecule, or controlling the oligomer length.[5] Another common strategy is incorporating electron-donating (D) and electron-accepting (A) groups into the molecular structure.[6] The choice and positioning of these D and A moieties can affect the energy levels, enabling control over the material's HOMO (highest occupied molecular orbital) and LUMO (lowest unoccupied molecular orbital) levels, as well as influencing its charge transfer characteristics.[7] Among D-A derivatives, the special class of D-A-D thiophene-based molecules has recently demonstrated utility in various applications. For instance, these molecules have been employed in the fabrication of single-

Chem. Eur. J. 2024, 30, e202303590 (1 of 10)

© 2023 The Authors. Chemistry - A European Journal published by Wiley-VCH GmbH

Chemistry–A European Journal | Research Article
doi.org/10.1002/chem.202303590

Chemistry
Europe
European Chemical
Societies Publishing

material organic solar cells (SMOSCs) and binary non-fullerene small-molecule organic solar cells (NF-SM OSCs), as well as in the development of electrochromic devices.[8] Furthermore, they have found use in developing fluorescent probes for visualizing protein dynamics or as active phototranducers within living cells.[9] Notably, D-A-D thiophene-based compounds are also known for their often considerable two-photon absorption (2PA) cross sections, which make them attractive as probes for two-photon (2P) microscopy.[10]

In this study, we present the synthesis of a new class of symmetrical D-A-D thiophene-based small molecules (*i.e.*, heptamers), showcasing their potential as near-infrared (NIR) emitting dyes and their multifunctionality/versatility in optoelectronic devices. As shown in Scheme 1, the π-conjugated molecules consist of electron-donating moieties, *i.e.*, a carbazole covalently linked to a monoalkylated bithiophene, end-capping a central electron acceptor unit with varying strength, *i.e.*, benzo[c][1,2,5]thiadiazole (**Bz**), thieno[3,4-b]pyrazine (**Pz**), and thieno[1,2,5]thiadiazole (**Tz**). In contrast to their **Bz** counterparts, materials containing **Tz** and **Pz** moieties have garnered comparatively less attention, suggesting the potential for untapped opportunities in optoelectronic applications.[11]

With the aid of Density Functional Theory (DFT) calculations, we elucidate the effect of the central acceptor unit on the redox and spectroscopic properties of the synthesized compounds. Within this family of materials, increasing the strength of the acceptor moieties (**Bz** < **Pz** < **Tz**), while keeping the donor (D) building blocks constant, enables the attainment of small molecular dyes emitting in the near-infrared. Notably, compounds containing **Pz** and **Tz** units exhibit: i) emission spectra in the NIR region (ranging from 700 to 1200 nm) and ii) low energy gaps (spanning from 1.6 to 1.4 eV), all while maintaining a relatively low-lying highest occupied molecular orbital (HOMO) energy level. Therefore, **Pz** and **Tz** stand out in their strong electron-acceptor capability compared to **Bz**, primarily owing to favorable ring structures for π-electron delocalization. Indeed, **Pz** and **Tz** units are directly connected to other rings through a thiophene moiety instead of a phenyl one, thus promoting an extended conjugation and facilitating charge transfer. Finally, we show that these materials exhibit multifunctional characteristics: from NIR electrochromic behavior to a unique ambivalent character in bulk heterojunction (BHJ) solar cells due to their ability to function as either active donors or
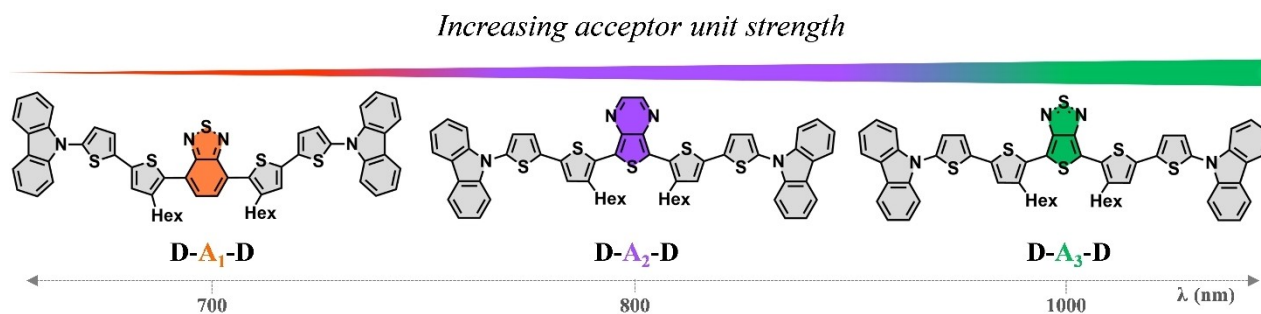
acceptors when combined with PCBM or P3HT, respectively. Additionally, DFT calculations suggest the suitability of these molecules as effective two-photon absorption (2PA) probes, thus further broadening their range of potential optoelectronic applications.
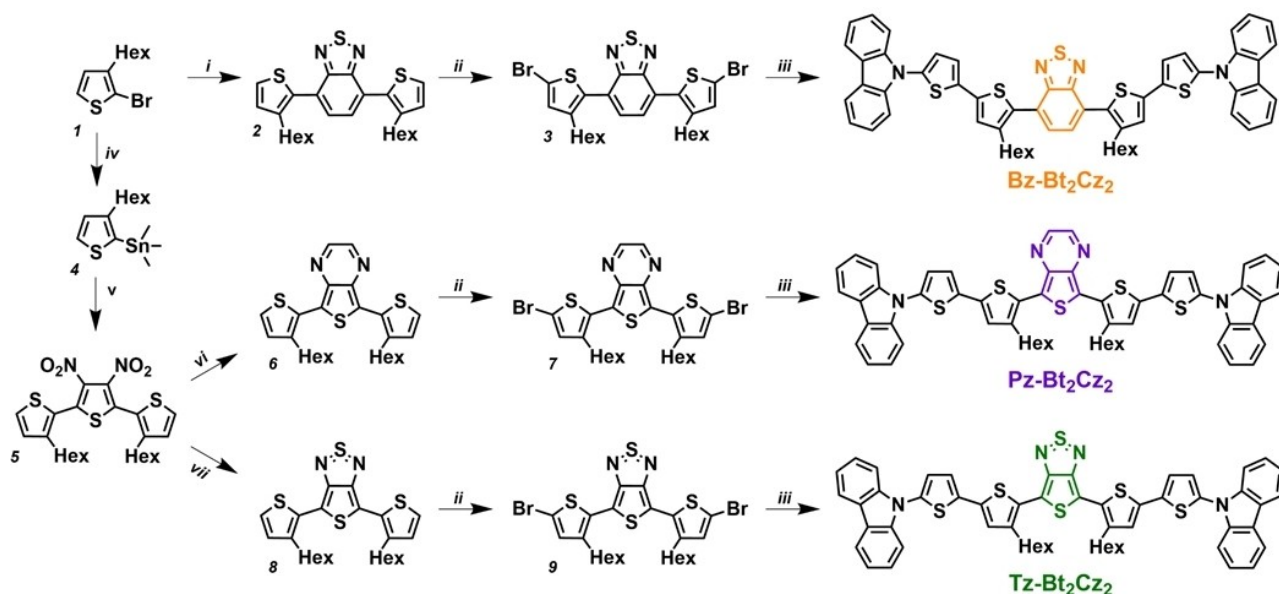
Results and Discussion

Synthesis and thermal characterizations

The synthetic methodology employed for synthesizing the three linear D-A-D oligomers, namely **Bz−Bt₂Cz₂**, **Pz−Bt₂Cz₂,** and **Tz−Bt₂Cz₂**, is outlined in Scheme 2.

As shown in the synthetic scheme, the initial step involved the preparation of central trimer cores (**2**, **6**, and **8**) integrating the acceptor units. This was achieved through cross-coupling reactions between the hexyl thiophene unit and the acceptor precursors.[12] The acceptor moieties, **Pz** and **Tz**, were formed by reducing the nitro groups of intermediate **5** and subsequently closing the heterocycle using appropriate reagents. Following this, the three inner cores containing the acceptor group (**3**, **7**, and **9**) were brominated and successively coupled *via* Stille reaction to the stannylated carbazole intermediate, resulting in the final D-A-D molecules (see Supplementary Information for details). All compounds were characterized by spectroscopic ¹H-NMR, ¹³C-NMR, mass spectrometry, and Fourier transform infrared (FTIR) analysis (Figures S1–S18). The strength of the acceptor units, which is determined by the presence of electronegative atoms and their different arrangement within the molecular unit, slightly impacted the yield of the cross-coupling reaction: the weaker the acceptor unit, the higher the yield. All oligomers in this configuration exhibit air stability and display good solubility in dichloromethane, chloroform, tetrahydrofuran, and toluene at room temperature, thanks to the alkylation of the two thiophene rings close to the central acceptor unit. Furthermore, differential scanning calorimetry (DSC) analysis was conducted to acquire insights into the impact of the substitution pattern on the thermal properties of the materials. As shown in Figure S19, all oligomers exhibit good thermal stability in an inert atmosphere, as they did not undergo any decomposition phenomena up to a temperature of 150 °C. Additionally, they do not display crystallinity and exhibit only a glass transition (Tg), suggesting their persistence in an

Increasing acceptor unit strength

D-**A₁**-D   D-**A₂**-D   D-**A₃**-D

700   800   1000   λ (nm)

Scheme 1. Molecular structures of the D-A-D oligomers.

Chemistry–A European Journal

Research Article
doi.org/10.1002/chem.202303590

Chemistry
Europe
European Chemical
Societies Publishing

i. *2,1,3-Benzothiadiazole-4,7-bis(boronic acid pinacol ester), NaHCO₃, Pd(dppf)Cl₂, THF/H₂O (2:1), 80°C;* **ii.** *NBS, CH₂Cl₂, 25°C;* **iii.** *9-(5-(trimethylstannyl)thiophen-2-yl)-9H-carbazole, Pd(PPh₃)₄, Toluene, 110°C;* **vi.** *2,5-dibromo-3,4-dinitrothiophene, Pd(PPh₃)₄, Toluene, 110°C;* **v.** *nBuLi, SnMe₃Cl, THF(dry), -78°C;* **vi.** *Fe(powder), CH₃COOH, Glyoxal (sol. 40% in H₂O), NaHCO₃, EtOH, 80°C;* **vii.** *Fe(powder), CH₃COOH, N-Thionylaniline, (CH₃)₃SiCl, Py(dry), 80°C.*

Scheme 2. Synthetic routes of **Bz–Bt₂Cz₂**, **Pz–Bt₂Cz₂**, and **Tz–Bt₂Cz₂**.

amorphous state over the investigated temperature range. According to classical conformational analysis, carbazole units should maintain an orthogonal orientation relative to the main molecular plane, thus disfavoring π-π stacking interactions between molecules and hampering efficient molecular packing.

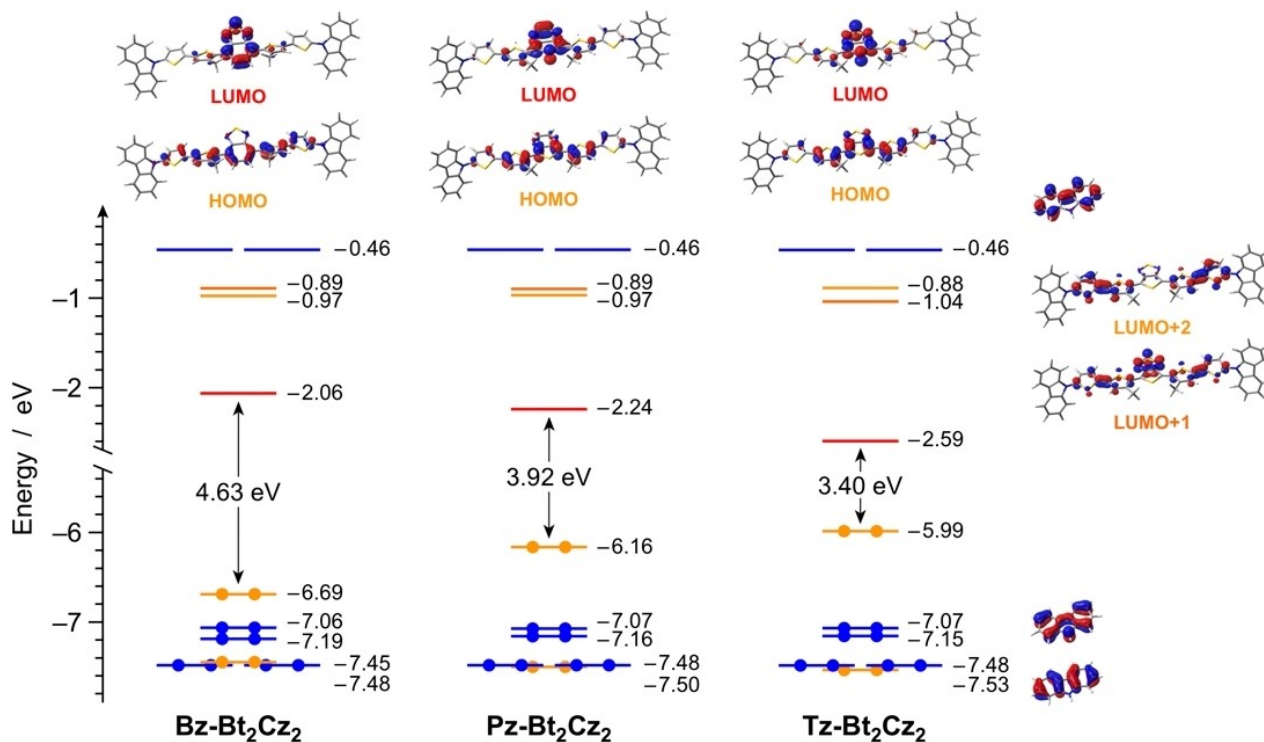Notably, the glass transition temperatures (Tg) of the different compounds present the following trend: 44.0 °C for **Bz–Bt₂Cz₂**, 73.0 °C for **Tz-CzBt₂**, 78.8 °C **Pz–Bt₂Cz₂** (Figure S19). These values indicate increased intermolecular interactions for **Tz-CzBt₂** and **Pz–Bt₂Cz₂** compared to **Bz–Bt₂Cz₂**. The data above support the observation that **Tz-CzBt₂** and **Pz–Bt₂Cz₂** compounds display reduced dihedral angles between the hexyl thiophene ring and the central acceptor moiety, as well as an enhanced quinoidal character, in comparison to **Bz–Bt₂Cz₂** (see next section).

DFT Calculations and Photophysics

To comprehensively understand the photophysical and electrochemical properties of **Bz–Bt₂Cz₂**, **Pz–Bt₂Cz₂**, and **Tz–Bt₂Cz₂**, all molecules were investigated by DFT and TD-DFT methods in dichloromethane as implicit solvent (see Supporting Information). All compounds exhibit high conformational freedom, with nearly isoenergetic minima in both C_2 and C_s symmetry. For the purpose of this study, the discussion will be focused on the C_s conformers, although an equivalent scenario can also be observed for C_2 counterparts. Comparing the geometry of the three molecules reveals that **Pz–Bt₂Cz₂** and **Tz–Bt₂Cz₂** exhibit a

higher coplanarity between the central acceptor units and the adjacent thiophene rings than **Bz–Bt₂Cz₂**, which instead displays an angle of 38.2° (Table S1). This difference is likely attributed to steric hindrance, as **Bz** is directly attached to other thiophene rings through a phenyl moiety, in contrast to **Pz** and **Tz**, which incorporate a thiophene group. Analyzing the angle between the two thiophene rings, specifically the one directly attached to the carbazole moiety and the one linked to the central acceptor unit, it is possible to observe a decrease along the series **Bz–Bt₂Cz₂**, **Pz–Bt₂Cz₂**, and **Tz–Bt₂Cz₂**, with values of 23.9°, 19.2°, and 15.5°, respectively (Table S1). This result can be ascribed to an enhancement of the quinoidal character, which increases in parallel to the strength of the central acceptor unit (**Bz** < **Pz** < **Tz**). Accordingly, the bond-length alternation (BLA)[13] of such dithiophene subunit in the three compounds (Figures S20–S21) corroborates this hypothesis. In all compounds, the terminal carbazole moieties adopt an almost perpendicular orientation relative to the outermost thiophene unit with an average dihedral angle of approximately 72°, favoring rigid H-shaped molecular structures (Table S1). As a result of this conformational arrangement, a notably weak coupling between the carbazole orbitals and the π-conjugated system of the thiophene-based oligomer is observed, as clearly illustrated by the topology of the frontier molecular orbitals in **Bz–Bt₂Cz₂**, **Pz–Bt₂Cz₂**, and **Tz–Bt₂Cz₂**, reported in Figure 1.

Considering the frontier molecular orbitals within the HOMO-5 to LUMO+4 range, only the HOMO and LUMO energies are strongly perturbed by changing the acceptor unit strength. In contrast, all other molecular orbitals retain their

Chemistry–A European Journal

Research Article
doi.org/10.1002/chem.202303590

Chemistry Europe
European Chemical
Societies Publishing

Figure 1. Energy diagram showing the energy values of the frontier Kohn-Sham molecular orbitals of **Bz–Bt₂Cz₂**, **Pz–Bt₂Cz₂**, and **Tz–Bt₂Cz₂** in dichloromethane. For relevant orbitals, the corresponding isosurfaces are also displayed for clarity (isovalue = 0.04 e$^{1/2}$ bohr$^{-3/2}$). Orbitals with similar topology are plotted with the same color for easier comparison (*e.g.*, carbazole-based orbitals are reported in blue and displayed in a compact way using pristine 9*H*-carbazole as a model compound).

topologies and energies, confirming that the carbazole moiety is decoupled from the oligothiophene chain.

In all molecules, the HOMO is primarily delocalized between the central acceptor moiety and the nearby thiophene rings, while the LUMO is almost exclusively centered on the former, leading to its gradual stabilization as the acceptor strength increases (*i.e.*, by 0.18 and 0.53 eV in **Pz–Bt₂Cz₂** and **Tz–Bt₂Cz₂** respectively, if compared to **Bz–Bt₂Cz₂**). Since the HOMO is conversely destabilized along the series, a substantial reduction in the HOMO-LUMO gap is observed (*i.e.*, 4.63, 3.92 and 3.40 eV for **Bz–Bt₂Cz₂**, **Pz–Bt₂Cz₂** and **Tz–Bt₂Cz₂**, respectively).
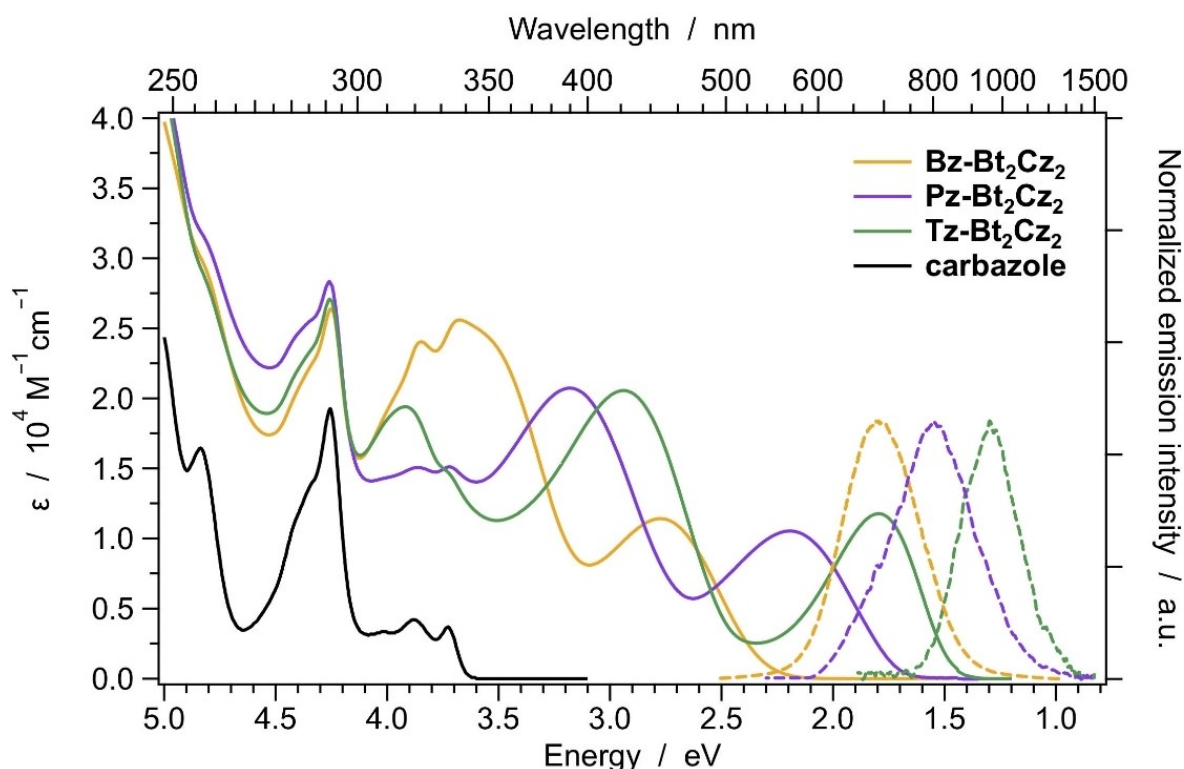
On the contrary, LUMO+1 and LUMO+2 orbitals are spread on all the thiophene units, and their energy levels remain relatively unaffected along the whole series (Figure 1). In these molecules, the lack of coupling between the peripheral carbazole units and the inner backbone results in molecular orbitals centered on these peripheral parts being well below the HOMO and above the LUMO levels, with virtually no energy change along the series. Consequently, the active involvement of the carbazole units in the electrochemical and excited-state processes at low energy can be ruled out.

Figure 2 reports the absorption spectra of **Bz–Bt₂Cz₂**, **Pz–Bt₂Cz₂**, and **Tz–Bt₂Cz₂** in solution. All molecules display a broad and unstructured absorption band at low energy, with maxima at 447 nm for **Bz–Bt₂Cz₂**, 565 nm for **Pz–Bt₂Cz₂**, and 690 nm for **Tz–Bt₂Cz₂**. Such intense transition ($\varepsilon \approx 1.1$ 10^4 M^{-1} cm^{-1} for all dyes) is exclusively attributed to the S₀→S₁ excitation resulting from a HOMO→LUMO transition, as con-

firmed by TD-DFT calculations (Figure S22 and Tables S2–S4). This lowest-energy absorption displays a considerable charge-transfer characteristic, promoting one electron from the central moiety and the nearby thiophene units to the π* orbitals of the central acceptor. Such a transition is estimated to occur at 2.88, 2.23, and 1.81 eV for **Bz–Bt₂Cz₂**, **Pz–Bt₂Cz₂**, and **Tz–Bt₂Cz₂**, respectively, as predictable from their decreasing HOMO-LUMO energy gap (see Figure 1). It is worth empathizing that this theoretical estimation is in excellent agreement with the experimental spectra, displaying band maxima at 2.77, 2.19, and 1.80 eV for **Bz–Bt₂Cz₂**, **Pz–Bt₂Cz₂** and **Tz–Bt₂Cz₂**, respectively (Figure S22).

The second energy absorption band is energetically well-separated from the S₀→S₁ transition, but it is still broad and unstructured, with maxima at 337, 390, and 422 nm for **Bz–Bt₂Cz₂**, **Pz–Bt₂Cz₂**, and **Tz–Bt₂Cz₂**, respectively (Figures 2 and S22). For all molecules, this absorption band is almost exclusively a result of the HOMO→LUMO+1 transition (compare Figure 1 and Tables S2–S4). This excitation process leads to the population of the S₂ state in **Tz–Bt₂Cz₂** and S₃ state for **Pz–Bt₂Cz₂** and **Bz–Bt₂Cz₂**. Indeed, in the latter cases, the S0→S2 excitations show very low oscillator strengths (f < 0.04, tables S2–S3), attributed, in the case of **Pz–Bt₂Cz₂**, to an n-π* transition resulting from nitrogen lone pairs accessible on the central portion, while in the case of **Bz–Bt₂Cz₂** to a poor orbital overlap.

At λ < 350 nm, the absorption features of **Bz–Bt₂Cz₂**, **Pz–Bt₂Cz₂** and **Tz–Bt₂Cz₂** display close similarities to the

Chemistry–A European Journal

Research Article
doi.org/10.1002/chem.202303590

Chemistry Europe
European Chemical
Societies Publishing

Figure 2. Absorption (full) and emission (dashed) spectra of **Bz–Bt$_2$Cz$_2$** (orange line), **Pz–Bt$_2$Cz$_2$** (violet line), and **Tz–Bt$_2$Cz$_2$** (green line) in dichloromethane solution at 298 K. For comparison, the absorption spectrum of unsubstituted 9H-carbazole is also reported.

absorption spectrum of pristine carbazole, with a virtually identical vibronic progression (Figure 2). It should be noted that TD-DFT calculations also indicate the existence of several middle- and long-range charge-transfer transitions with low oscillator strengths (i.e., $f < 0.02$, see Tables S2–S3), which are experimentally not detectable.

As shown in Figure 2, **Bz–Bt$_2$Cz$_2$**, **Pz–Bt$_2$Cz$_2$**, and **Tz–Bt$_2$Cz$_2$** display room-temperature fluorescence. All emission bands are broad and unstructured, with photoluminescence quantum yields of 0.357, 0.008, and 0.003 for **Bz–Bt$_2$Cz$_2$**, **Pz–Bt$_2$Cz$_2$** and **Tz–Bt$_2$Cz$_2$**, respectively. Notably, **Tz–Bt$_2$Cz$_2$** stands out as a virtually complete near-infrared emitting dye with an emission band ranging from 800 to 1200 nm and peaking at 950 nm. Due to the large energy gap between S$_1$ and higher-lying excited states (Figure S22 and Tables S2–S4), it can be confidently assumed that regardless of excitation wavelength, all compounds readily relax to S$_1$, which is in turn the emissive state. Accordingly, the emission profile is the mirror image of the S$_0$→S$_1$ absorption band. Nevertheless, a considerable Stokes shift is experimentally observed (i.e., 0.98, 0.65, and 0.50 eV for **Bz–Bt$_2$Cz$_2$**, **Pz–Bt$_2$Cz$_2$**, and **Tz–Bt$_2$Cz$_2$**, respectively). TD-DFT optimization of the S$_1$ geometry reveals that all molecules undergo an overall flattening upon excited-state relaxation (Figure S21 and Table S1). In their S$_1$ minima, both **Pz–Bt$_2$Cz$_2$** and **Tz–Bt$_2$Cz$_2$** experience a virtually complete planarization of their oligothiophene backbone, comprehending the peripheral carbazole moieties which reduce their dihedral angle to approximately 60° (Figure S21 and Table S1). This observation

suggests that **Tz–Bt$_2$Cz$_2$**, which exhibits a smaller Stokes shift than **Pz–Bt$_2$Cz$_2$**, already displays a considerable quinoidal character in its ground state (Figure S20). On the other hand, **Bz–Bt$_2$Cz$_2$** is unable to achieve full planarization of its backbone even in the S$_1$ excited state because of the steric hindrance between the benzothiadiazole acceptor and the nearby thiophene ring. Nevertheless, the angle between such two planes reduces from 38.2° in S$_0$ to 12.2° in S$_1$ (resulting in a variation of 26° compared to a variation of just 0.5° in **Pz–Bt$_2$Cz$_2$** and **Tz–Bt$_2$Cz$_2$**, since already coplanar). Accordingly, the remarkable excited-state flattening observed in **Bz–Bt$_2$Cz** can be responsible for its larger Stokes shift experimentally observed.

Finally, TD-DFT results suggest that **Bz–Bt$_2$Cz$_2$**, **Pz–Bt$_2$Cz$_2$**, and **Tz–Bt$_2$Cz$_2$** could display notable two-photon absorption cross-sections, as already found for similar thiophene-based D-A-D systems.[10] By comparing the orbital topologies of the TD-DFT calculations on the present systems with the smaller analogs,[10a] it can be inferred that the bright one-photon S$_0$→S$_1$ transition will display a negligible two-photon absorption cross-section (δ_{2PA}) for all the molecules. On the contrary, increasingly high δ_{2PA} values are probable for the S$_0$→S$_2$ transition in **Bz–Bt$_2$Cz$_2$**, S$_0$→S$_5$ in **Pz–Bt$_2$Cz$_2$**, and both S$_0$→S$_3$ and S$_0$→S$_4$ excitations in **Tz–Bt$_2$Cz$_2$**. Moreover, by looking at the Natural-Transition-Orbital pairs (NTOs) of these transitions (Tables S2–S4), it is evident that the related orbitals are always well spread all along the molecular backbone; indeed since the delocalization degree of the NTOs is known to be strongly correlated to

Chemistry–A European Journal

Research Article
doi.org/10.1002/chem.202303590

Chemistry
Europe
European Chemical
Societies Publishing

the two-photon absorption cross-section of the associated transition,[14] superior δ_{2PA} values are expected for all the investigated dyes, if compared to previously published analogous.

Electrochemistry and spectroelectrochemistry in solution and thin film

Figure 3a compares the cyclic voltammograms (CVs) for the three molecules in solution, and Table 1 provides summarized data. Additionally, Figure S24 illustrates their CVs at different scan rates.

As shown in Figure 3a, **Bz—Bt$_2$Cz$_2$** exhibits a quasi-reversible oxidation at 0.93 V (with peak-to-peak potential differences ranging from 0.07 to 0.16 V) and reduction wave at −1.34 V (with a peak-to-peak potential difference of 0.2 V). In comparison, **Pz—Bt$_2$Cz$_2$** and **Tz—Bt$_2$Cz$_2$** exhibit less sharp and quasi-reversible oxidation waves at lower potentials, 0.71 V and 0.67 V, respectively, in agreement with their enhanced electron-accepting characteristics. The increase in electron affinity of the two molecules is further evidenced by the shift of the reduction
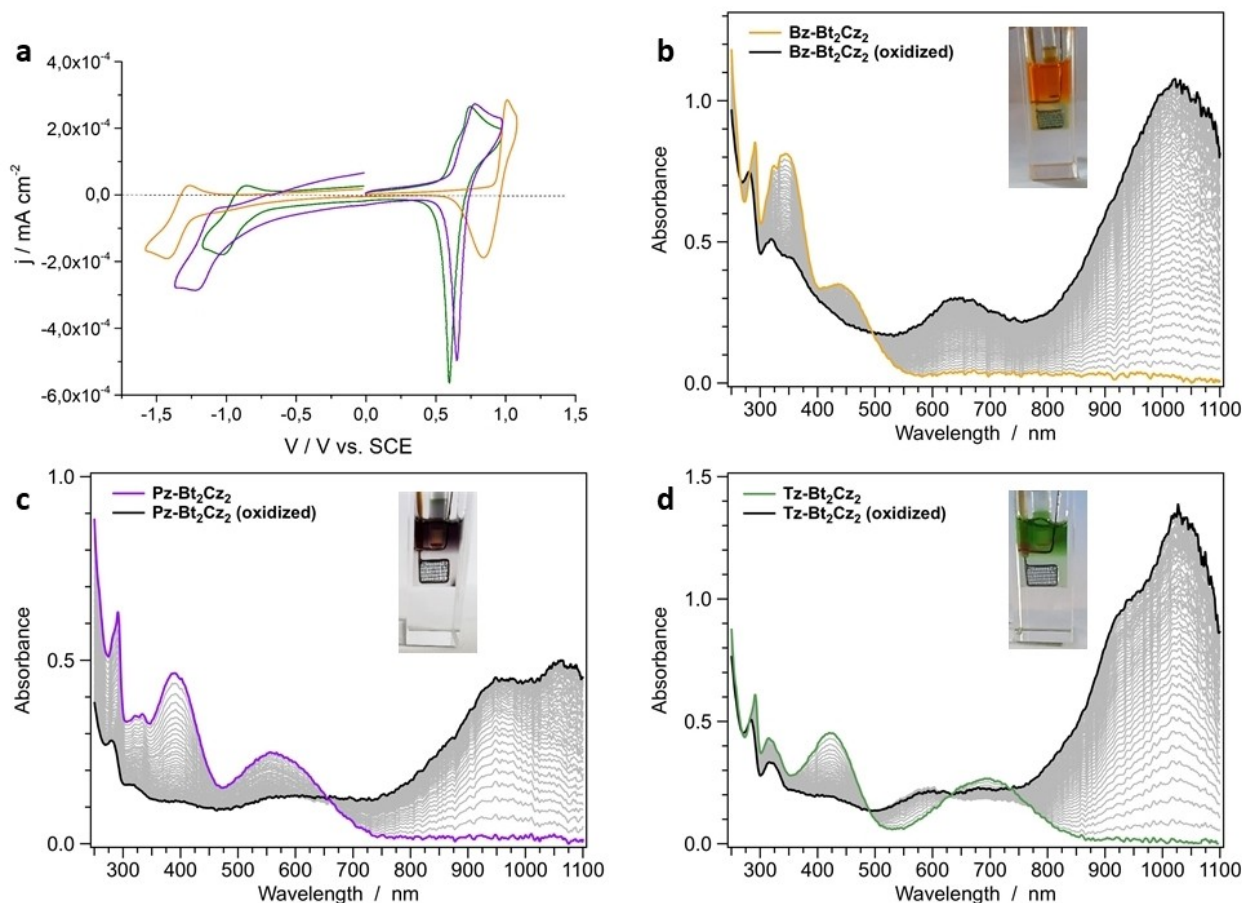
Figure 3. (a) Cyclic voltammograms at a scan rate of 100 mV s^{-1} and (b–d) spectroelectrochemical experiments at a constant voltage of $(E°_{ox} + 0.1)$ V vs. SCE. Both measurements were carried out in dichloromethane solution at 298 K; color code: **Bz—Bt$_2$Cz$_2$** (orange), **Pz—Bt$_2$Cz$_2$** (violet), and **Tz—Bt$_2$Cz$_2$** (green).

Table 1. Redox potentials vs. SCE, HOMO-LUMO levels, and energy gap of **Bz—Bt$_2$Cz$_2$**, **Pz—Bt$_2$Cz$_2$**, and **Tz-CzBt$_2$**.

Molecule	Electrolyte	$E°_{ox}$/V	$E°_{red}$/V	HOMO/eV	LUMO/eV	E_g^{elect}/eV
CH$_2$Cl$_2$ Solution						
Bz—Bt$_2$Cz$_2$	$(C_4H_9)_4NClO_4$	0.93	−1.34	5.61	3.34	2.27
Pz—Bt$_2$Cz$_2$	$(C_4H_9)_4NClO_4$	0.71	−1.15	5.39	3.53	1.86
Tz—Bt$_2$Cz$_2$	$(C_4H_9)_4NClO_4$	0.67	−0.94	5.35	3.74	1.61
Thin film in propylene carbonate						
Bz—Bt$_2$Cz$_2$	$(C_2H_5)_4NBF_4$	0.84	−1.16	5.52	3.52	2.00
Pz—Bt$_2$Cz$_2$	$(C_2H_5)_4NBF_4$	0.65	−0.95	5.33	3.72	1.61
Tz—Bt$_2$Cz$_2$	$(C_2H_5)_4NBF_4$	0.59	−0.84	5.27	3.84	1.43

Chemistry–A European Journal

Research Article
doi.org/10.1002/chem.202303590

Chemistry Europe
European Chemical
Societies Publishing

waves toward less negative potentials. Specifically, as indicated by the peak-to-peak differences, quasi-reversible peaks shifted at -1.15 V for **Pz−Bt$_2$Cz$_2$** and -0.94 V for **Tz−Bt$_2$Cz$_2$** are observed (see SI for more details), thus leading to a drastic reduction in the energy gap of approximately 0.4–0.6 eV, in agreement with DFT calculations.

All compounds display a huge variation in their color upon oxidation, as clearly visible by monitoring the change in their absorption spectra upon application of a constant voltage of $(E°_{ox} + 0.1)$ V *vs.* SCE in dichloromethane solution (Figure 3b–d).

Indeed, spectroelectrochemical experiments show an overall bleaching of the lowest-energy absorption bands of all molecules and the appearance of a broad and intense absorption band at $\lambda > 800$ nm, extending up to the NIR region. Thanks to unrestricted DFT and TD-DFT calculations carried out on the oxidized radical cation of **Tz−Bt$_2$Cz$_2$**, such a band is attributed to a transition taking place in the NIR region (*i.e.*, at 1150 nm for **Tz−Bt$_2$Cz$_2$$^+$**) involving an electronic excitation from the thiophene units to the central acceptor (Figure S23). However, in the case of **Bz−Bt$_2$Cz$_2$**, oxidation also leads to the appearance of a second band within the wavelength range of 550 to 750 nm; consequently, the radical cation of **Bz−Bt$_2$Cz$_2$** exhibits a greenish color, as depicted in Figure 3b (inset). On the contrary, the oxidized forms of **Pz−Bt$_2$Cz$_2$** and **Tz−Bt$_2$Cz$_2$** appear nearly transparent in the visible range, particularly for **Pz−Bt$_2$Cz$_2$**, making them attractive electrochromic materials (Figure 3c–d, inset).

Electrochemical analyses were also performed on thin films in propylene carbonate (PC) with $(C_2H_5)_4NBF_4$ 0.1 mol L^{-1} as a supporting electrolyte. In the solid state, all molecules show sharp and quasi-reversible oxidation waves, in line with the trend observed in the solution (Figure S25 and Table 1). Indeed, the onset potentials of **Pz−Bt$_2$Cz$_2$** film (0.65 V) and **Tz−Bt$_2$Cz$_2$** film (0.59 V) result close to each other and significantly less positive than that of **Bz−Bt$_2$Cz$_2$** (0.87 V). At negative potentials, only **Bz−Bt$_2$Cz$_2$** films exhibit quasi-reversible reduction waves, with the latter showing the lowest reduction potential (-0.84 V for **Tz−Bt$_2$Cz$_2$** < -0.95 V for **Pz−Bt$_2$Cz$_2$** < -1.16 V for **Bz−Bt$_2$Cz$_2$**. The relative HOMO and LUMO energy levels, calculated from the onset of the oxidation and reduction wave, respectively, are reported in Table 1.

The ability of **Pz−Bt$_2$Cz$_2$** and **Tz−Bt$_2$Cz$_2$** to switch from a colored (neutral) to an uncolored (oxidized) state in solution was further explored in thin films to assess their potential application in electrochromic devices.[15] Thin films of **Pz−Bt$_2$Cz$_2$** and **Tz−Bt$_2$Cz$_2$** blended with a 5% of HydrinC to enhance ion conduction within the organic film[16] were prepared and tested (Figure S26). In both cases, the spectral changes observed upon electrochemical oxidation were reversible, fast, and consistent with the measurement in solution. Only minor broadening of the absorption bands was observed with respect to dichloromethane solution measures (compare Figure 3c–3d with S26a–S26b), suggesting that the loose solid-state molecular packing, caused by the encumbered H-shape of these molecules, has little impact on their electrochromic properties.

Photovoltaic characteristics

Due to the interesting optoelectronic characteristics of these compounds, we conducted further investigations to explore their photovoltaic properties in bulk heterojunction (BHJ) organic solar cells (see Supporting Information for the device fabrication). Given that their energy levels lie between those of P3HT and PCBM, we assessed their possible bifunctional behavior (*i.e.*, their ability to either donate or accept electrons when blending with PCBM and P3HT).[4a] Table 2 provides a comprehensive summary of the photovoltaic data, and the corresponding J–V features of the best-performing solar cells curves are reported in Figure 4.

All molecules exhibit photoactive properties when blended in a 1:1 ratio with PCBM. **Pz−Bt$_2$Cz$_2$** showed the highest power conversion efficiencies (PCE) due to enhancements of Jsc and FF values, which align with the broader absorption spectra of the blends in thin film (Figure S27) and enhanced morphological characteristics. In-depth investigations of the morphology of the active layers, conducted through FE-SEM measurements, highlight that films containing **Pz−Bt$_2$Cz$_2$** molecules exhibit superior uniformity and smoother surfaces in contrast to films incorporating **Bz−Bt$_2$Cz$_2$** and **Tz−Bt$_2$Cz$_2$** (Figure S28). However, further refinements of the thin film morphology (*i.e.*, by

Table 2. Short-circuit current density (J_{sc}), open-circuit voltage (V_{oc}), fill factor (FF), and power conversion efficiency (PCE) of tested BHJ solar cells.

Sample	J_{sc} (mA cm^{-2})	V_{oc} (V)	FF	PCE (%)
As donor materials				
Bz−Bt$_2$Cz$_2$:PCBM	5.06	0.56	0.41	1.16
Pz−Bt$_2$Cz$_2$:PCBM	6.75	0.55	0.52	1.93
Tz−Bt$_2$Cz$_2$:PCBM	5.25	0.51	0.48	1.28
As acceptor materials				
P3HT:Pz−Bt$_2$Cz$_2$	6.03	0.52	0.46	1.44
P3HT:Tz−Bt$_2$Cz$_2$	5.22	0.44	0.51	1.17
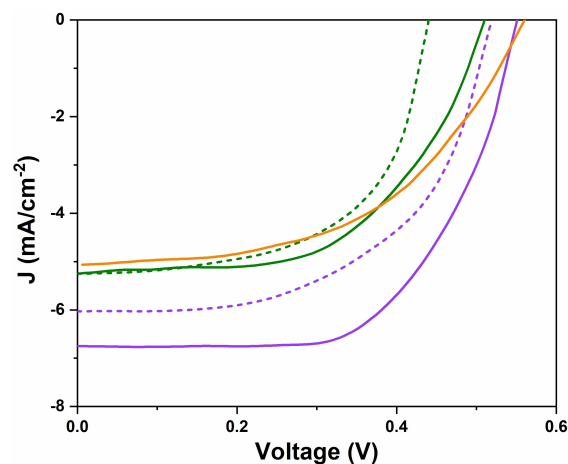
Figure 4. J-V curves of the cells fabricated using blends of **Bz−Bt$_2$Cz$_2$** (orange curve), **Pz−Bt$_2$Cz$_2$** (violet curve), and **Tz−Bt$_2$Cz$_2$** (green curve) with PCBM (solid line) or P3HT (dashed line).

Chemistry–A European Journal

Research Article
doi.org/10.1002/chem.202303590

**Chemistry
Europe**
European Chemical
Societies Publishing

optimizing the solvent employed for deposition, adjusting the photoactive materials ratio, refining deposition methods, *etc.*) are essential to prevent the observed nanosegregation, thereby enhancing film homogeneity and possibly power conversion efficiency (PCE) values.[17]

Differently, not all oligomers were effective as acceptor materials when blended with P3HT in a 1:1 ratio. In this case, only **Pz-CzBt₂** and **Tz-CzBt₂** yielded discernible photoconversion, primarily attributed to their more stable LUMO energy levels and improved film morphology (Figure S29), with the former exhibiting the highest efficiency owing to their better Jsc and Voc values. These measurements highlight the bifunctional characteristics of the oligomers containing either **Pz** or **Tz** functional groups, underscoring their potential as versatile materials for diverse photovoltaic applications.

Conclusions

In this study, we have successfully synthesized and characterized a novel family of thiophene-based small molecules featuring a D-A-D sequence. Our investigation, complemented by Density Functional Theory (DFT) calculations, shed light on the profound impact of three distinct acceptor units – benzo[c][1,2,5]thiadiazole (**Bz**), thieno[3,4-b]pyrazine (**Pz**), and thieno[1,2,5]thiadiazole (**Tz**) – when combined with electron donor units derived from carbazole thiophene derivatives. Our findings reveal that the incorporation of **Pz** and **Tz** moieties induces a significant planarization of the oligomeric inner core, both in the ground (S_0) and excited (S_1) states. This is attributed to their enhanced quinoidal character, as corroborated by bond-length alternation (BLA) analysis, which significantly influences their (opto)electronic properties and opens up numerous potential applications.

The demonstrated NIR electrochromic behavior, two-photon absorption (2PA), and ambivalent characteristics in BHJ solar cells make these molecules promising candidates for next-generation energy-efficient and multifunctional optoelectronic devices. Future research directions could include further optimization of their chemical structure in order to tailor their electronic structure to achieve even more efficient charge transfer.

Experimental section

Reagents and materials. TLC were carried out with 0.2-mm thick of silica gel 60 F254(Sigma). Preparative column chromatographies were carried out on glass columns with silica gel 60 (particle sizes 0.040–0.063 mm, Sigma). 3-hexylthiophene, 4,7-bis(4,4,5,5-tetramethyl-1,3,2-dioxaborolan-2-yl)benzo[c][1,2,5]thiadiazole, N-bromosuccinimide (NBS), n-butyllithium 2.5 M solution in hexane, tributyltin chloride, 2,5-dibromo-3,4-dinitrothiophene, iron powder, glyoxal (sol. 40% in H_2O), N-thionylaniline, chlorotrimethylsilane, 2-bromothiophene, 9H-carbazole, CuI, NaHCO₃, glacial CH_3COOH, Cs₂CO₃, tetrakis(triphenylphosphine)palladium(0) Pd(PPh₃)₄, [1,1′-Bis(diphenylphosphino)ferrocene] dichloropalladium(II) Pd(dppf)Cl₂ were purchased from Merck. All reagents and solvents were used as received. Organic solvents were dried by standard procedures.

Microwave experiments were carried out in a CEM Discover SP-Microwave Synthesizer reactor in a closed vessel (230 W, fixed temperature at 80°C, air, high stirring rate). All ^1H NMR and ^{13}C NMR spectra were recorded on a Varian Mercury-400/500 spectrometer equipped with a 5-mm probe. Chemical shifts were calibrated using the internal CDCl3 resonance, which were referenced to TMS. Mass spectra were collected on a Thermo Scientific TRACE 1300 gas chromatograph. Differential scanning calorimetry (DSC) was performed under nitrogen on a DSC TA Instruments Q2000, operating in the −50 to 150°C temperature range at a heating scan rate of 10°C min⁻¹. FTIR analysis were performed using an Agilent Cary 630 FTIR.

Photophysical Measurements. Spectroscopic investigations were performed in spectrofluorimetric grade dichloromethane using fluorimetric Suprasil quartz cuvettes (path length: 10.00 mm). Absorption spectra were recorded with a PerkinElmer Lambda 950 spectrophotometer. Uncorrected emission spectra were obtained with an Edinburgh Instruments FLS920 spectrometer equipped with a Peltier-cooled Hamamatsu R928 photomultiplier tube (PMT, spectral window: 185–850 nm) and a super-cooled (193 K) Hamamatsu R5509-72 PMT for the near-infrared region (spectral window: 550–1650 nm). An Osram XBO xenon arc lamp (450 W) was used as an excitation light source. Corrected spectra were acquired by means of a calibration curve obtained using an Ocean Optics deuterium-halogen calibrated lamp (DH-3plus-CAL-EXT). Photoluminescence quantum yields (PLQYs) in solution were obtained from the corrected spectra on wavelength scale (nm) and measured according to the approach described by Demas and Crosby, using an air-equilibrated water solution of [Ru(bpy)₃]Cl₂ (PLQY = 0.040) as reference. Experimental uncertainties are estimated to be ±10% for PLQYs, ±2 nm, and ±5 nm for absorption and emission peaks, respectively.

DFT Calculations. Density functional theory (DFT) calculations were carried out using the B.01 revision of the Gaussian 16 program package,[18] in combination with the M06-2X hybrid meta exchange-correlation functional,[19] which has been specifically designed to work well with charge-transfer excitations having intermediate spatial overlap.[20] For all atoms, the Pople 6-31+G(d) basis set was adopted, as implemented in Gaussian 16, as a good compromise between accuracy and computational cost.[21] The polarizable continuum model (PCM) was employed to take into account dichloromethane solvation effects.[22] All calculations were performed within both the C_2 and C_s point-group symmetry, resulting in nearly isoenergetic minima in the ground state ($\Delta E < 4$ meV); accordingly, only data within the C_s symmetry will be discussed since no substantial differences were observed for the C_2 conformers. TD-DFT calculations, at the same level of theory used for ground-state optimizations, were used to compute Franck-Condon excitations and to fully optimize the lowest-energy excited state (S_1) of all molecules.[23] Analytical frequency calculations at both DFT and TD-DFT levels were always carried out to confirm the nature of the stationary points on the potential energy surfaces. All the pictures of molecular orbitals and density surfaces were created using GaussView 6.[24]

Cyclic voltammetry (CV) measurements. CVs of **Bz−Bt₂Cz₂**, **Pz−Bt₂Cz₂**, and **Tz−Bt₂Cz₂** were performed at room temperature in solution 0.5 mmol L⁻¹ purged with Ar by using AMEL model 5000 Electrochemical System at scan rates from 0.20 to 0.01 V s⁻¹ in a three-compartment glass electrochemical cell with Pt disk working electrode (diameter 1 mm) and Pt wire auxiliary electrode. The electrolytic solution contains 0.1 mol L⁻¹ (C₄H₉)₄NClO₄ (Fluka puriss., recrystallized from CH₃OH and stored under reduced pressure in a dryer filled with CaCl₂) in CH₂Cl₂ (distilled over P₂O₅ and stored under Ar pressure). The reference electrode was aqueous KCl Saturated Calomel Electrode (SCE), and, in this supporting electro-

Chemistry–A European Journal

Research Article
doi.org/10.1002/chem.202303590

Chemistry Europe
European Chemical
Societies Publishing

lyte, the ferricinium/ferrocene potential is 0,47 V vs. SCE. HOMO and LUMO energy levels were evaluated according to Reference [25]. All compounds were drop cast from CH_2Cl_2 on the Pt disk working electrodes (diameter 1 mm) to obtain modified electrodes that were successively tested in another three-compartment glass electrochemical cell with a Pt wire auxiliary electrode. The electrolytic solution for modified electrode testing was 0.1 mol L^{-1} $(C_2H_5)_4NBF_4$ (Aldrich for electrochemical analysis > 99.0%, stored in $CaCl_2$ dryer under reduced pressure) in propylene carbonate (Aldrich, anhydrous 99.7%) where the three oligomers are not soluble; in this supporting electrolyte, the ferricinium/ferrocene potential is 0,50 V vs. SCE.

Spectroelectrochemistry. Spectroelectrochemical measurements were carried out using a Metrohm AutoLab PGSTAT 302 N electrochemical work-station (equipped with the NOVA 2.1.6 software package), combined with a coupled deuterium-halogen lamp (Avantes AvaLight-DHc) and an Avantes Starline spectrometer (AvaSpec ULS2048CL-EVO-RS, detection range: 200–1100 nm), controlled by AvaSoft 8.14. Measurements in solution were carried out at room temperature in dichloromethane with 0.1 M tetrabutylammonium hexafluorophosphate (electrochemical grade, TBAPF$_6$) as the supporting electrolyte. Solid-state measurements were executed at 298 K on thin films dipped in propylene carbonate with 0.1 M lithium perchlorate (electrochemical grade, LiClO$_4$) as the supporting electrolyte. In both cases, oxygen was removed from the solutions by bubbling nitrogen. All the experiments were carried out using a three-electrode setup using a suitably shaped platinum working electrode, aqueous Ag/AgCl reference electrode, and a platinum wire as the counter electrode.

Device fabrication. The Indium Tin oxide (ITO) substrate (2.0×2.0 cm, surface resistance 21 Ω/sq) was etched at 60 °C for 15 min by using a 10%wt aq. solution of HCl, to obtain an active area of 1.5×1.0 cm. The substrate was rinsed with distilled water, 2-propanol and dried before use. The solution of poly(3,4-ethylenedioxythiophene):polystyrene sulfonic acid (PEDOT:PSS, 2.8 wt% dispersion in water, viscosity 20 cps) in 2-propanol (diluted 1:1 v/v) was sonicated for 30 min using an ultrasonic bath (Elmasonic S 30H), filtered on a Gooch G2 and then deposited by doctor blading technique (Sheen Instrument Model S265674) onto the previously treated ITO substrate, only leaving a small (0.5×1.0 cm) area uncovered at the opposite side of the previously etched area. The PEDOT:PSS film was annealed at 120 °C for 1 h and 30 min under vacuum (Buchi GKR-50 glass oven, 10^{-3} mmHg). A solution made by mixing 2.5 mg of heptamer and 2.5 mg of PC$_{61}$BM or P3HT [Poly(3-hexylthiophene), HT 96%, Mn 30.0 kD, PDI 1.2, synthesized starting from 3-hexylthiophene through GRIM Method][26] in 0.5 mL of chlorobenzene was sonicated for 30 min and subsequently deposited by the aforementioned doctor blading technique on the slide in order to cover the PEDOT:PSS layer. The sample was then annealed in the glass oven under vacuum (10^{-3} mmHg) at 120 °C for 30 min. Finally, ~50 nm of Al was thermal evaporated using an Edwards 6306 A coating system operating at 10^{-6} mmHg. The structure of the final devices, having a final active area of 1.0×1.0 cm^2, was composed of ITO (80 nm)/PEDOT:PSS (100 nm)/photoactive layer (150 nm)/Al (50 nm).

Field emission scanning electron microscope (FE-SEM). In order to accurately investigate the morphological properties of the developed structures, the surface features of the fabricated polymer-based films were examined using a FE-SEM (Crossbeam 350, Zeiss, Germany). The morphological studies were carried out at a working distance of 5 mm and accelerating voltage of 5 kV using the SE2 detector to collect high-resolution micrographs at two different magnification levels (i.e., ×20000 and ×50000). Before the investigation, the samples were sputtered with gold layers of 8 nm

thickness using an SC7620 Polaron mini sputter coater (Quorum Technologies Ltd., Ashford, UK).

Acknowledgements

Conflict of Interests

The authors declare no conflict of interest.

Data Availability Statement

The data that support the findings of this study are available on request from the corresponding author. The data are not publicly available due to privacy or ethical restrictions.

[1] a) J. Chen, W. Zhang, L. Wang, G. Yu, *Adv. Mater.* **2023**, *35*, 2210772; b) B. Kan, Y. Kan, L. Zuo, X. Shi, K. Gao, *InfoMat.* **2021**, *3*, 175–200; c) C. J. Kousseff, R. Halaksa, Z. S. Parr, C. B. Nielsen, *Chem. Rev.* **2022**, *122*, 4397–4419; d) D. T. Christiansen, A. L. Tomlinson, J. R. Reynolds, *J. Am. Chem. Soc.* **2019**, *141*, 3859–3862.

[2] a) M. Sawatzki-Park, S. Wang, H. Kleemann, K. Leo, *Chem. Rev.* **2023**, *123*, 8232–8250; b) M. Cigànek, J. Richtàr, M. Weiter, J. Krajčovič, *Isr. J. Chem.* **2022**, *62*, e202100061.

[3] a) F. Zhang, D. Wu, Y. Xu, X. Feng, *J. Mater. Chem.* **2011**, *21*, 17590–17600; b) M. Zangoli, F. Di Maria, G. Barbarella, *ChemistryOpen.* **2022**, *9*, 499–511.

[4] a) M. Marinelli, A. Candini, F. Monti, A. Boschi, M. Zangoli, E. Salatelli, F. Pierini, M. Lanzi, A. Zanelli, M. Gazzano, F. Di Maria, *J. Mater. Chem. C.* **2021**, *9*, 11216–11228; b) G. Turkoglu, M. E. Cinar, T. Ozturk, *Top. Curr. Chem.* **2017**, *375*, 8.

[5] a) E. Salatelli, M. Marinelli, M. Lanzi, A. Zanelli, S. Dell'Elce, A. Liscio, M. Gazzano, F. Di Maria, *J. Phys. Chem. C.* **2018**, *122*, 4156–4164; b) C. L. Radford, P. D. Mudiyanselage, A. L. Stevens, T. L. Kelly, *ACS Energy Lett.* **2022**, *7*, 1635–1641; c) C. Bulumulla, R. Gunawardhana, R. Kularatne, M. E. Hill, G. T. McCandless, M. C. Biewer, M. C. Stefan, *ACS Appl. Mater. Interfaces.* **2018**, *10*, 11818–11825; d) Q. Zhao, D. Li, J. Peng, *Macromolecules.* **2023**, *56*, 490–500.

[6] X. Wan, C. Li, M. Zhang, Y. Chen, *Chem. Soc. Rev.* **2020**, *49*, 2828–2842.

[7] a) D. Hashemi, X. Ma, R. Ansari, J. Kim, J. Kieffer, *Phys. Chem. Chem. Phys.* **2019**, *21*, 789–799; b) H. Imahori, Y. Koboti, H. Kaji, *Acc. Chem. Res.* **2021**, *2*, 501–514; c) X. Chen, X. Zhang, Z. Wang, J. Zhao, *Angew. Chem.* **2023**, *135*, e202216010.

[8] a) R. Rybakiewicz-Sekita, P. Toman, J. Ganczarczyk, J. Drapala, P. Ledwon, M. Banasiewicz, L. Skorka, A. Matyjasiak, M. Zagorska, A. Pron, *J. Phys. Chem. B.* **2022**, *126*, 4089–4105; b) M. Marinelli, M. Lanzi, A. Liscio, A. Zanelli, M. Zangoli, F. Di Maria, E. Salatelli, *J. Mater. Chem. C.* **2020**, *8*, 4124–4132; c) F. Di Maria, M. Biasucci, F. P. Di Nicola, E. Fabiano, A. Zanelli, M. Gazzano, E. Salatelli, M. Lanzi, F. Della Sala, G. Gigli, G. Barbarella, *J. Phys. Chem. C.* **2015**, *119*, 27200–27211; d) A. Aubele, T. Kraus, S. Schmid, E. Mena-Osteritz, P. Bäuerle, *Chem. Eur. J.* **2023**, *29*, e2023015; e) X. Xu, Q. Peng, *Chem. Eur. J.* **2023**, *8*, e202104453.

[9] a) A. Cantelli, M. Malferrari, A. Soldà, G. Simonetti, S. Forni, E. Toscanella, E. J. Mattioli, F. Zerbetto, A. Zanelli, M. Di Giosia, M. Zangoli, G.

Chemistry–A European Journal

Research Article
doi.org/10.1002/chem.202303590

Chemistry Europe
European Chemical
Societies Publishing

Barbarella, S. Rapino, F. Di Maria, M. Calvaresi, *JACS Au.* **2021**, *1*, 925–935; b) M. Zangoli, F. Di Maria, *VIEW* **2021**, *2*, 20200086; c) J. Barsotti, S. Perotto, A. Candini, E. Colombo, F. V. A. Camargo, S. Di Marco, M. Zangoli, S. Sardar, A. J. Barker, C. D'Andrea, G. Cerullo, S. Rozen, F. Benfenati, F. Di Maria, G. Lanzani, *ACS Appl. Mater. Interfaces.* **2023**, *15*, 13472–13483; d) I.E. Palamà, F. Di Maria, M. Zangoli, S. D'Amone, G. Manfredi, J. Barsotti, G. Lanzani, L. Ortolani, E. Salatelli, G. Gigli, G. Barbarella, *RSC Adv.* **2019**, *9*, 23036–23044; e) M. Zangoli, A. Cantelli, A. Candini, A. Lewinska, F. Fardella, A. Tino, G. Tommasini, M. Wnuk, M. Moschetta, S. Perotto, M. Lucarini, C. Tortiglione, G. Lanzani, F. Di Maria, *J. Phys. Chem. C.* **2023**, *127*, 4672–4683; f) L. Lantz, H. Shirani, T. Klingstedt, K. R. Nilsson, *Chem. Eur. J.* **2020**, *26*, 7425–7432; g) B. A. D. Neto, J. R. Correa, J. Spencer, *Chem. Eur. J.* **2022**, *28*, e202103262.

[10] a) S. Canola, L. Mardegan, G. Bergamini, M. Villa, A. Acocella, M. Zangoli, L. Ravotto, S. A. Vinogradov, F. Di Maria, P. Ceroni, F. Negri, *Photochem. Photobiol. Sci.* **2019**, *18*, 2180–2190; b) M. Fan, G. Chen, Y. Xiang, J. Li, X. Yu, W. Zhang, X. Long, L. Xu, J. Wu, Z. Xu, Q. Zhang, *Chem. Eur. J.* **2021**, *27*, 10898–10902; c) S. David, H–J. Chang, C. Lopes, C. Brännlund, B. Le Guennic, G. Berginc, E. Van Stryland, M. V. Bondar, D. Hagan, D. Jacquemin, C. Andraud, O. Maury, *Chem. Eur. J.* **2021**, *27*, 3517–3525.

[11] a) Y. Li, J. Sun, M. Chen, S. Miao, M. Liu, Y. Ma, G. Wang, X. Gu, B. Z. Tang, *Adv. Funct. Mater.* **2022**, *32*, 2205494; b) Y. Li, J. Gao, S. Wang, S. Li, X. Hou, Y. Pan, J. Gao, X. Qiao, Z. Tian, D. Chen, H. Deng, Z. Deng, X. Hong, Y. Xiao, *J. Controlled Release* **2022**, *342*, 157–169; c) M. B. Desta, N. S. Vinh, C. H. P. Kumar, S. Chaurasia, W. T. Wu, J. T. Lin, T. C. Wei, E. W. G. Diau, *J. Mater. Chem. A.* **2018**, *6*, 13778–13789; d) S. Steinberger, A. Mishra, E. Reinold, E. Mena-Osteritz, H. Müller, C. Uhrich, M. Pfeiffer, P. Bäuerle, *J. Mater. Chem.* **2012**, *22*, 2701–2712.

[12] F. Di Maria, B. Barbarella, *J. Sulfur Chem.* **2013**, *34*, 627–637.

[13] H. Yanai, Y. Terajima, F. Kleemiss, S. Grabowsky, T. Matsumoto, *Chem. Eur. J.* **2023**, *29*, e202203538.

[14] C.-L. Sun, Q. Liao, T. Li, J. Li, J.-Q. Jiang, Z.-Z. Xu, X.-D. Wang, R. Shen, D.-C. Bai, Q. Wang, S.-X. Zhang, H.-B. Fu, H.-L. Zhang, *Chem. Sci.* **2015**, *6*, 761–769.

[15] a) T. Moreira, F. Di Maria, M. Zangoli, E. Fabiano, I. Manet, R. Mazzaro, V. Morandi, M. Marinelli, G. Gigli, A. J. Parola, C. A. T. Laia, G. Barbarella, *Adv. Electron. Mater.* **2021**, *7*, 2100166; b) T. Moreira, C. A. T. Laia, M. Zangoli, M. Antunes, F. Di Maria, S. De Monte, F. Liscio, A. J. Parola, G. Barbarella, *ACS Appl. Polym. Mater.* **2020**, *2*, 3301–3309.

[16] N. Munichandraiah, L. G. Scanlon, R. A. Marsh, *J. Appl. Electrochem.* **1994**, *24*, 1066–1072.

[17] C. Cui, Y. Li, *Aggregate.* **2021**, *2*, 31.

[18] M. J. Frisch, G. W. Trucks, H. B. Schlegel, G. E. Scuseria, M. A. Robb, J. R. Cheeseman, G. Scalmani, V. Barone, G. A. Petersson, H. Nakatsuji, X. Li, M. Caricato, A. V. Marenich, J. Bloino, B. G. Janesko, R. Gomperts, B. Mennucci, H. P. Hratchian, J. V. Ortiz, A. F. Izmaylov, J. L. Sonnenberg, D. Williams-Young, F. Ding, F. Lipparini, F. Egidi, J. Goings, B. Peng, A. Petrone, T. Henderson, D. Ranasinghe, V. G. Zakrzewski, J. Gao, N. Rega, G. Zheng, W. Liang, M. Hada, M. Ehara, K. Toyota, R. Fukuda, J. Hasegawa, M. Ishida, T. Nakajima, Y. Honda, O. Kitao, H. Nakai, T. Vreven, K. Throssell, J. A. Montgomery Jr., J. E. Peralta, F. Ogliaro, M. J. Bearpark, J. J. Heyd, E. N. Brothers, K. N. Kudin, V. N. Staroverov, T. A. Keith, R. Kobayashi, J. Normand, K. Raghavachari, A. P. Rendell, J. C. Burant, S. S. Iyengar, J. Tomasi, M. Cossi, J. M. Millam, M. Klene, C. Adamo, R. Cammi, J. W. Ochterski, R. L. Martin, K. Morokuma, O. Farkas, J. B. Foresman, D. J. Fox, *Gaussian 16, Revision B.01*, Gaussian, Inc, Wallingford, CT, USA **2016**.

[19] a) Y. Zhao, D. G. Trulhar, *Theor. Chem. Acc.* **2008**, *120*, 215–241; b) Y. Zhao, D. G. Trulhar, *Acc. Chem. Res.* **2008**, *41*, 157–167.

[20] R. Li, J. Zheng, D. G. Truhlar, *Phys. Chem. Chem. Phys.* **2010**, *12*, 12697–12701.

[21] T. Clark, J. Chandrasekhar, G. W. Spitznagel, P. Von Ragué Schleyer, *J. Comput. Chem.* **1983**, *4*, 294–301.

[22] J. Tomasi, B. Mennucci, R. Cammi, *Chem. Rev.* **2005**, *105*, 2999–3093.

[23] a) C. Adamo, D. Jacquemin, *Chem. Soc. Rev.* **2013**, *42*, 845–856; b) A. D. Laurent, C. Adamo, D. Jacquemin, *Phys. Chem. Chem. Phys.* **2014**, *16*, 14334–14356; c) M. Mayer, S. Kruger, N. Rosch, *J. Chem. Phys.* **2001**, *115*, 4708–4717.

[24] GaussView, Version 6, R. Dennington, T. A. Keith, J. M. Millam, Semichem Inc., Shawnee Mission, KS, USA **2016**.

[25] S. Trasatti, *Pure Appl. Chem.* **1986**, *58*, 955–966.

[26] R. S. Loewe, P. C. Ewbank, J. Liu, L. Zhai, R. D. McCullough, *Macromolecules* **2001**, *34*, 4324.